Retrospective Theses and Dissertations

Iowa State University Capstones, Theses and Dissertations

2008

# Computational studies on the effect of water impact on an unmanned air vehicle

Gregory Zink
*Iowa State University*

Follow this and additional works at: https://lib.dr.iastate.edu/rtd

Part of the Aerospace Engineering Commons

Computational studies on the effect of water impact on an Unmanned Air Vehicle

by

Gregory Zink

A thesis submitted to the graduate faculty

in partial fulfillment of the requirements for the degree of

MASTER OF SCIENCE

Major:  Aerospace Engineering

Program of Study Committee:
Tom I.P. Shih, Major Professor
Thomas J. Rudolphi
Mark Bryden

Iowa State University

Ames, Iowa

2008

# TABLE OF CONTENTS

UMI Number: 1453112

# UMI®

# LIST OF FIGURES

# LIST OF TABLES

# ABSTRACT

Computational Fluid Dynamics (CFD) was used in conjunction with Finite Element Analysis (FEA) to simulate the water splashdown and effects thereof on an Unmanned Air Vehicle (UAV). The CFD simulation utilized time-accurate finite-volume code to model both "compressible" and "incompressible" ensemble averaged Navier- Stokes equations. The model also incorporated the volume of fluid method to track the air-water interface, and dynamic cell remeshing to move the UAV body through the computational domain. The model was verified by comparing pressure histories with experimental test data. There was good agreement in character and magnitude of these results, with some deviance in the inlet duct of the aircraft. Tests were performed for various drop heights, yielding different impact velocities. Finally, the CFD results were used to perform an FEA study of the effect on the inlet close-off door. As confirmed by experimental test hardware, the FEA model predicted that the door would permanently deform, requiring reinforcement to the support arm.

# CHAPTER 1.  INTRODUCTION

Lockheed Martin is currently developing an Unmanned Aerial Vehicle (UAV) concept that is launched from and recovered by a submerged nuclear submarine.  Such an aircraft presents several unique engineering challenges, among them the splashdown into the water.  The UAV has been designed to descend with the aid of a parachute, nose-first into the ocean.  Although the use of the parachute slows the aircraft before entry, the forces on impact are still significant and could adversely affect the structure of the vehicle.

Water entry has been studied analytically in the past, primarily in the work of Von Karman and Wagner.  However, their work focused on simple shapes, and employed simplifications such as ignoring compressibility effects.  For many objects, this is an acceptable means of analysis, but not so for Lockheed's UAV.  Since it is a functional aircraft, the geometry of the vehicle has been designed for aerodynamics first, and thus presents a complex shape.  Also, the engine inlet duct traps air between the UAV and the water surface, which tends to compress the air.  Modeling the complex physics acting on an intricate shape requires a computational solution.

While a fluid simulation can provide pressures acting on the aircraft body, it does not give any indication of the potential damage the UAV components might experience at impact.  Thus the results of the simulation must be connected to a structural analysis tool to obtain a complete understanding of the splashdown physics.

The overall goal of this study was to determine the effects on the UAV when it entered the water nose-first prior to being retrieved by the submarine.  This involved simulating the splashdown at various impact velocities and investigating the pressure field,

deceleration history and overall fluid behavior.  This data was then fed into a structural analysis to quantify the stresses induced in the component materials.  With this collection of data, predictions could be made about the aircraft's ability to survive the water impact forces.

Computational analyses were performed for both fluid dynamic and structural studies of the UAV.  All fluid dynamics simulations were performed in Fluent 6.2 commercial CFD code, and the stresses were modeled in ANSYS Workbench 11.0 commercial FEA software package.  The CFD portion of this effort was done in collaboration with Andrew Wick at Iowa State University; the continuation in FEA analysis was done independently by this author.

# CHAPTER 2.  PROBLEM FORMULATION

## 2.1  Setup

A CAD file of the aircraft geometry was provided by Lockheed Martin.  The model was of the UAV forebody, consisting of the nose, air inlet duct, forward fuselage, and leading edge of the wings.  Figure 1 shows this portion of the aircraft.  Only the forward section was modeled to aid in computational cost, and to mirror physical testing planned by Lockheed Martin, also using only the UAV forebody.
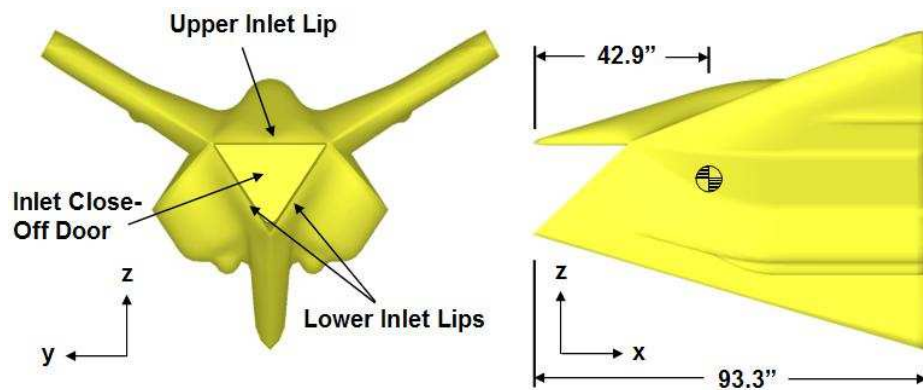


**Figure 1.  UAV Forebody**

The UAV's engine is protected from the elements at water splashdown by a triangular duct with an engine close-off door.  The door is composed of an inflatable seal sandwiched between two titanium panels, as shown in Figure 2.  The seal ensures that no corrosive seawater enters the engine to damage the delicate components.  Note that this figure shows the test article configuration, with rigid attachment to the aircraft body via 3 door mounts. The actual UAV features a single pivoting mechanism as depicted in the sketch also shown in Figure 2.  Here a piston extends as the door rotates about its hinge to swing shut.
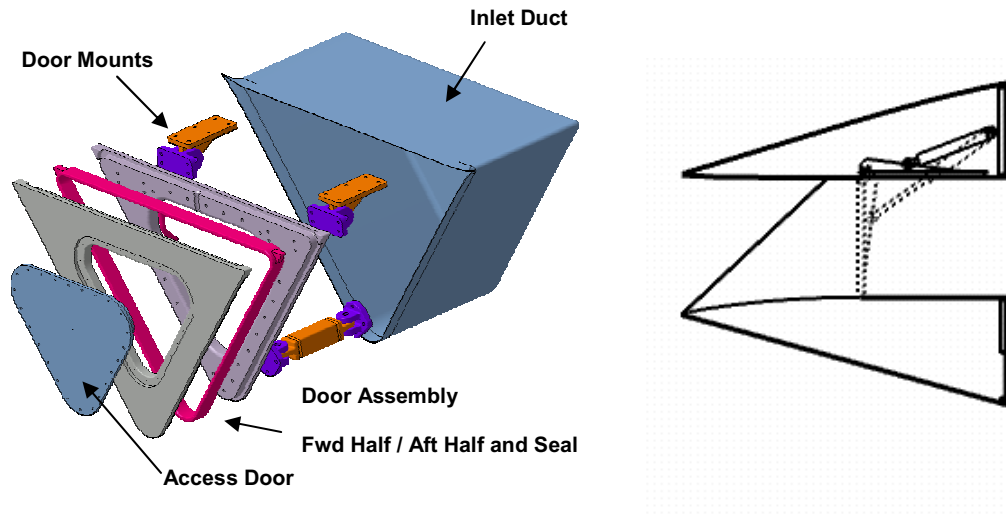
**Figure 2. Inlet Door Geometry**

For the CFD analysis the aircraft was initially placed above the water at a prescribed

distance, measured from the free surface to the tip of the UAV nose. Several different

heights were analyzed, each yielding a different impact velocity. In order to make the

computational models as accurate as possible, mass and material data were applied to the

UAV, and atmospheric conditions to the domain. Wherever possible, this data matched the

actual aircraft or test day atmosphere. These properties are given in Tables 1 and 2 below.

**Table 1. Mass Properties**

| Weight | 4148 lb |
|--------|---------|
| $I_{xx}$ | 261.5 slug ft$^2$ |
| $I_{yy}$ | 514.6 slug ft$^2$ |
| $I_{zz}$ | 552.6 slug ft$^2$ |
| Door Mat'l | Ti-64 |
| Arm Mat'l | Stainless Steel |

**Table 2. Fluid Properties**

| | Air | Water |
|--|-----|-------|
| Density, $\rho_\infty$ | 0.00233 slug/ft$^3$ | 1.9791 slug/ft$^3$ |
| Temp, $T_\infty$ | 531.3° R | 531.3° R |
| Pressure, $p_\infty$ | 14.7346 psi | $\rho_\infty gh$ |
| Viscosity, $\mu_\infty$ | 3.755x10$^{-7}$ slug/ft s | 2.095x10$^{-5}$ slug/ft s |

## 2.2 Assumptions

The splashdown simulations achieved the desired impact velocities by dropping the UAV from rest at a height above the water's surface. Generally the aircraft was oriented with the nose pointed directly at the free surface, with no angular displacement or velocity. However, for those cases where experimental test data was available, the initial orientation was prescribed prior to releasing the body. Note that this was only an initial position, and all motion was induced by gravity and the pressure field.

The effects of surface tension were neglected for the CFD models. This was deemed an acceptable simplification due to the relatively large magnitude of the Weber Number, defined in Eq. (1). A typical guideline states that when the Weber Number is greater than 100, surface tension effects can be neglected. For the problem of the UAV splashdown, with an impact velocity of 64.7 ft/s, a characteristic length equal to the length of the forebody, and water tension, $\sigma$, of 4.98 x $10^{-9}$, Weber Number is computed to be 1.301 x $10^{7}$, far beyond the range where surface tension is significant. Additionally, the air portion of the domain was initialized with uniform properties throughout, but hydrostatic pressure was used in the water.

$$We = \frac{LV_{impact}^2\rho_\infty}{g\sigma} \qquad (1)$$

For the structural model, linear elastic properties were initially used for the entire door mechanism, including the titanium and stainless steel components. Any nonlinear parameters were modeled using a multilinear isotropic hardening (MISO) model. All materials were assumed to be isotropic for all studies.

## 2.3  Governing Equations

The unsteady "compressible" ensemble averaged Navier-Stokes equations were used to model the air behavior, while the unsteady "incompressible" ensemble averaged Navier-Stokes equations were used in the water portion of the domain.  The one-equation Spalart-Allmaras turbulence model with wall functions was used in both media, and the Volume of Fluid (VOF) model was used to control the free surface between them.  The FEA model employed both linear elastic and nonlinear structural finite element formulations to model the structural effects.

## 2.4  Boundary and Initial Conditions

The computational domain was defined as an open container, half filled with water.  The sides and bottom of the domain were selected to be adiabatic walls, to contain all of the water and not allow it to flow out.  A pressure boundary was used on the upper surface to prevent a closed system and allow for inflow or outflow of air.  The UAV itself was modeled as a rigid adiabatic surface.

Initially, there was no velocity present in either fluid, standard atmospheric pressure in the air, and hydrostatic pressure in the water.  Temperature was initialized to $531.9°$ R throughout the domain to match the test day conditions.  A small amount of turbulent viscosity $\nu_t = 1 \times 10^{-5}$ ft$^2$/s was added for use with the turbulence model.

For the FEA model, the edges of the door were modeled as frictionless supports, allowing the door only to translate within the duct area.  The end of the support arm was cylindrically fixed, only allowing the arm to rotate as the door displaced.  At the pin joint connecting the arm to the door contact elements were used.  This allowed the forces of the

impact to be transmitted between the components, while still allowing them to pivot with respect to one another.

# CHAPTER 3.  GRID TOPOLOGY

In making the computational grid, the domain was first split into two parts.  The first of these was a cylindrical outer grid, extending to the far-field boundaries.  The cylinder had a radius of 58 ft and a height of 176 ft.  A split line was incorporated at the midpoint of this height to map the water's surface.  A cylinder of this size allowed for the splashdown to be simulated without boundary influences affecting the solution.

Within the cylindrical outer grid, a spherical subgrid was built around the aircraft geometry.  The sphere had a radius of 25 ft, and was located within the cylinder such that the UAV would be at the center of the outer domain at impact.  The UAV was surface meshed with rectangular cells, which then were mapped out to the sphere using hexahedral cells. This allowed for clustering close to the UAV surface and high resolution of the pressure field near the aircraft body, yielding a more accurate result.

Just outside the 25 ft sphere was another layer 8 ft thick, comprised of tetrahedral cells.  This was designed to be a transition layer between the fine hexahedral grid within the sphere and the coarser tetrahedral grid of the outer cylindrical domain.  The entire grid is shown in Figure 3, and the local surface mesh is shown in Figure 4.

The grid was constructed in this manner to allow the use of a cell remeshing technique to model the splashdown dynamics.  In this scheme, described in more detail in Chapter 4, the spherical grid traversed through the cylindrical outer grid.  The outer cells deformed as the sphere moved, until they reached a criterion where the outer grid was remeshed.  Utilizing this method, the spherical hexahedral grid around the body remained

intact throughout the simulation, and the effects of remeshing were localized far from the aircraft geometry.
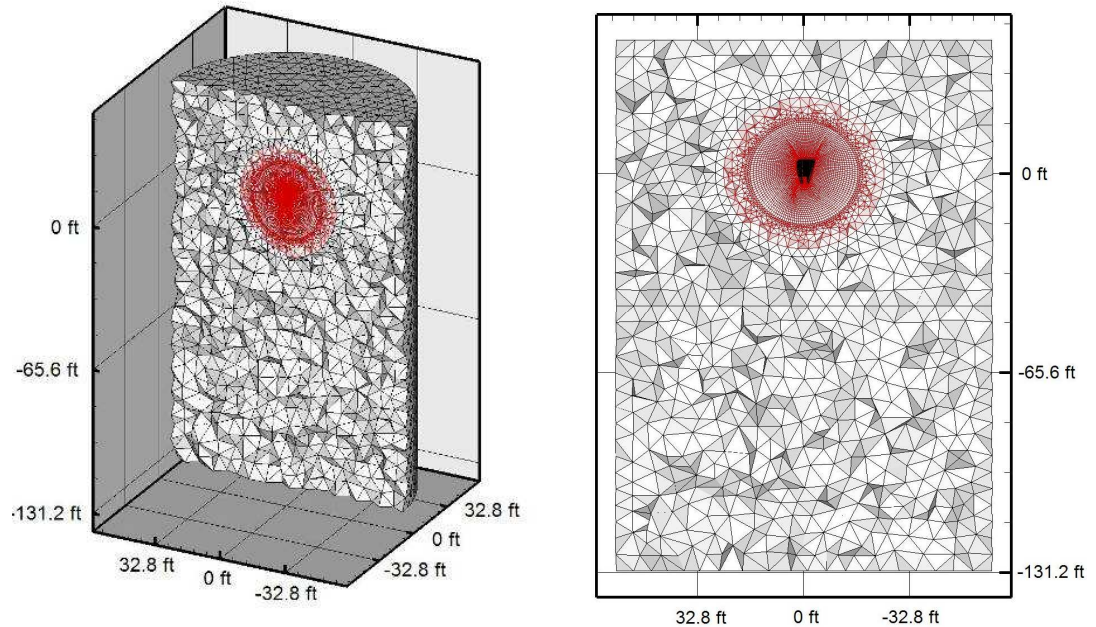


**Figure 3.  Baseline Grid Topology**

This general topology was used, but special attention was paid to the cells within the boundary layer.  The first cell length outward from the surface of the UAV was 0.3 in, selected to provide a wall y+ value of 40 for the 40 ft drop case.  This allowed the use of wall functions in Fluent's turbulence model.  Since the flow was not uniform, though, this y+ value was not maintained at all points in the grid for all times.  Specifically near the inlet door, where air velocities were highest and air compressibility effects were prominent, the value increased.  This was an unavoidable source of error, and deemed acceptable for this study.
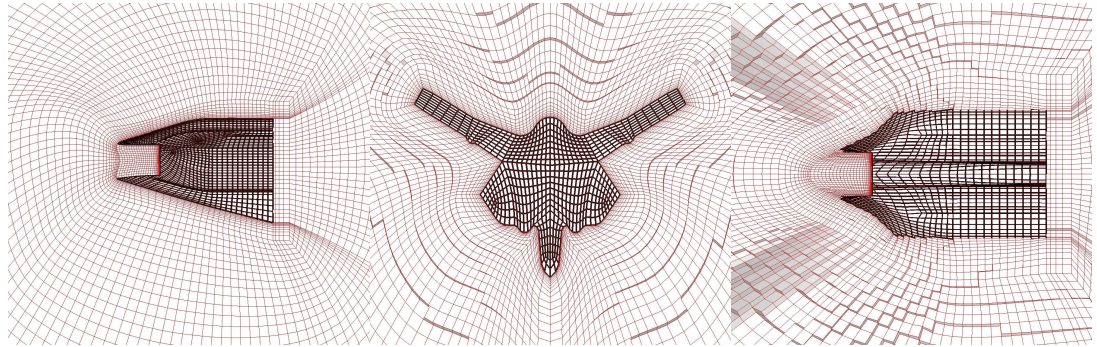
**Figure 4. Near-Body Grid Detail**

In solid mechanics, there is no equivalent of the boundary layer, so the focus of mesh generation was on areas of fine geometric detail and regions where high stresses were expected. The finite element mesh was built in ANSYS using a mix of tetrahedral and hexahedral elements, with sizing independently chosen for the various components. Clustering was done initially at the expected high stress locations, and refined after an initial analysis. This mesh is shown in Figure 5.



**Figure 5. Finite Element Analysis Mesh**

# CHAPTER 4.  NUMERICAL METHODS OF SOLUTION

With the meshes created, it was necessary to choose the specific numerical tools to solve the splashdown problem.  Most vital of these methodologies were the need to model the UAV's motion as it fell toward the water, and the need to accurately simulate the behavior of the water from impact to vehicle submergence.  A dynamic cell remeshing algorithm was used to move the UAV through the grid, while the water surface was characterized by a volume of fluid model.  Additionally, non-iterative time advancement was used with variable time-stepping to accurately solve the actual fluid equations with the proper time step size.  Details of these methods are given in the following sections.

## 4.1  Dynamic Cell Remeshing

The dynamics of the splashdown problem are unique in the complex motions of the aircraft as it approaches, impacts, and sinks into the water.  Modeling this mandated that the UAV be dropped from a height above the surface, and that the splashdown translational and rotational motion be purely dictated by the fluid equations.  This means that the UAV needed to be free to move throughout the meshed computational domain.

The cell remeshing algorithm used to achieve this dynamic model first was given a nondeforming region (the UAV) and an outer deforming mesh region.  The UAV kept its face mesh intact as it moved through the grid, distorting the attached cells in either compression or extension.  As these cells became more and more stretched or compressed, they surpassed a threshold for either mesh size or skew, and the algorithm rebuilt the outer mesh.  The flow solution from the prior mesh at the most recent time step was then projected onto the new remeshed grid for the next step.

This algorithm is powerful in that it allows actual motion to be captured, but it has limitations at the areas where the grid is remeshed. Projection errors occur when interpolating from a deformed mesh to a new mesh, particularly at the boundary where the cells were stretched or compressed. Clustering of grid points is also difficult, since the algorithm fails if the body moves more than one cell per time step.

To use dynamic remeshing but not be limited by its inaccuracies, a two-part grid was built. A spherical nondeforming mesh was built around the UAV, and this sphere moved with the aircraft as it fell. This moved the boundary, and hence the effects of remeshing, out from the surface of the UAV to the junction between the nondeforming and deforming meshes. The small inaccuracies where remeshing took place were now far enough from the UAV that they did not affect the pressure field near the aircraft, where measurements were being taken.

The actual motion of the UAV was determined using a six degree-of-freedom solver to integrate the pressures and shear forces acting on the body. This was done for each time-step, determining the UAV's position for the next step. This determination of the future location of the UAV by the present time step necessitated the use of a first-order solver for motion.

## 4.2  Volume of Fluid Model

The water surface which the UAV splashed into was modeled using the Volume of Fluid (VOF) method. In this type of simulation, the air and water are computationally treated as one fluid, with the momentum, energy and turbulence equations shared through both phases. The air and water are differentiated from one another by a free-surface discontinuity.

The position and motion of this surface are independent of the grid, so the water surface can pass through computational cells, without the need to be aligned with cell edges. At each time-step, the continuity equation is used to compute a volume fraction, determining the quantity of air and water in each cell. A discretization scheme uses this information to then set the shape of the water free surface.

## 4.3  Non-Iterative Time Advancement

To speed the solution process, a non-iterative time advancement scheme was used, employing the Fractional Step method. The difference between this method and a typical iterative process is in the order of the solution. An iterative solver computes the solution to the continuity, momentum and energy equations once per iteration, and continues to iterate until they are converged. Non-iterative time advancement segregates these equations, and solves them independently until each is converged for a given time step. That is, the continuity equation is solved to a converged value, then the momentum equation is solved, followed sequentially by the energy, turbulence and free surface volume fraction equations.

The act of segregating the equations in this way introduces a splitting error not present in a coupled iterative solution. The non-iterative scheme must then perform sub-iterations on each equation until the splitting error is of the same order as the inherent truncation error of the numerical scheme. However, the sum of these sub-iterations is still less than the number of global iterations for an iterative procedure, so the scheme decreases computational time. The addition of an Algebraic Multi-Grid solver also sped up the solution process at each sub-iteration.

## 4.4  Discretization Schemes

In general, the highest-order, most stable discretization schemes were used wherever possible to solve the fluid dynamic equations.  For the convective terms of momentum, energy and turbulence, the third-order MUSCL scheme was used.  For the pressure term, solution stability concerns led to the use of a body-force weighted scheme.  This method assumes a constant normalized gradient between the pressure and body forces to calculate face pressures, and was the best suited scheme to the effects of gravity on the UAV.  Density discretization was of high importance for this multiphase simulation, especially near the water's surface, where the density gradient was largest.  A first-order upwind scheme was used due to the aforementioned requirement of the cell remeshing technique that this term be first-order accurate.

Computation of the free-surface shape required two different schemes to be used during the solution, for stability reasons.  The most accurate method is geometric reconstruction, where the interface is defined as linear in each cell.  This creates a piecewise linear free surface across the domain with a sharp discontinuous transition from air to water. The geometric reconstruction scheme was employed during the UAV's fall through the air, and as the nondeforming grid passed through the water's surface.

Unfortunately, this scheme proved to be unstable just as the UAV impacted the water, due to the high velocities seen as the air rushed away from the gap between the aircraft and the water.  Therefore, the surface tracking scheme was changed to Euler-explicit just before impact.  This scheme uses the cell volume fraction and face fluxes to computes the free surface shape using a finite-differencing method.  However, the use of finite-difference causes the sharp free surface to become diffused across several cells near the interface.  This

effect was lessened by the use of the High Resolution Interface Capturing (HRIC) scheme to compute the finite difference. HRIC uses NVD methods with both upwind and downwind differencing to define a free surface that is much less diffused than other finite-difference schemes.

## 4.5 Variable Time-Stepping

The splashdown problem presented a unique issue for the selection of time-step for the solution. The moment of impact produced the highest flow velocities, with air being displaced at very high speeds, at the nose region of the aircraft, where the computational grid was finest. This necessitated the use of very small time-steps, as the solution became unstable if the water surface crossed more than one cell per time step. However, it was impractical to use such small time-steps during free-fall, where the free surface was unaffected by the UAV. This led to the use of a variable time-stepping method.

The variable time-stepping scheme computes a maximum Δt for each time step based on a user-specified maximum cell flux-based Courant Number. This relation is shown in Eq. (2). The Courant Number then dictates how far the water surface is allowed to move per time step, with a value of 1 being equivalent to one cell's distance per time-step. With this prescribed Courant Number (nu=1), the solution then was able to determine the maximum allowable time step.

$$\Delta t_{global} = \frac{\nu_{flux}}{\max \Sigma \left( \frac{outgoing fluxes}{volume} \right)} \qquad (2)$$

# CHAPTER 5.  RESULTS AND DISCUSSION

The initial simulations were performed for verification purposes, to ensure that the grid resolution was sufficient to accurately model the flow physics.  With confidence in the computational model, a parametric study was done, varying the aircraft drop height to determine trends in the results.  These were then compared to experimental test results to validate the model.

## 5.1  Verification

Grid sensitivity studies were performed for the case of the UAV dropped from rest from 40 ft.  This height was selected because it was the desired design point for Lockheed Martin's test article, and since it was the maximum height of all simulated cases.  This made it the "worst-case" scenario, with the aircraft seeing the highest velocities and pressures during the splashdown.  The grid described in Chapter 2 served as the baseline.  To create a "fine" grid, the number of grid cells was doubled in all three mapped directions.  Similarly, a "coarse" grid was made by halving the number of cells in each direction.  Since the doubling and halving of the mesh density occurred in all directions, the effect on overall cell count was eightfold, giving three distinct levels of mesh refinement.  These are given in Figure 6.  Note also that time-step is a function of the grid size, using variable time-stepping, so grid independence implies time-step independence.
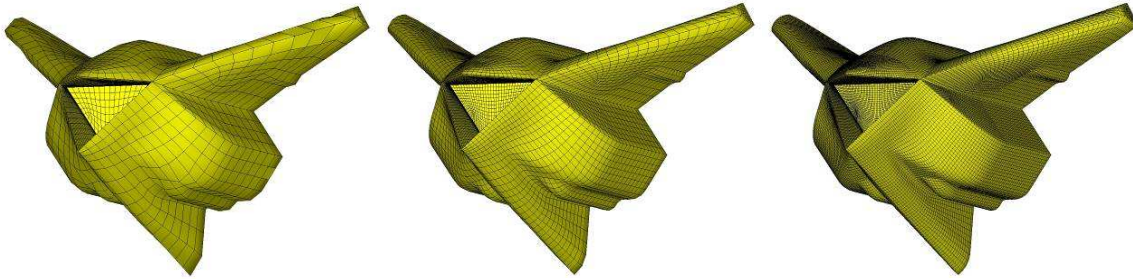
**Figure 6. Surface Mesh for Coarse, Medium, and Fine Grids**

For the splashdown problem, the forces acting on the UAV are the most important output parameter, so the verification study focused on them as a measure of grid independence. Specifically, the upward force, or what could be referred to as the drag force, was compared between the three grids for any sign of deviation. Plots of the drag force are shown in Figure 7 below. Note that the time-history of the drag force is broken up into three plots, to illustrate finer differences that might be overlooked on the overall scale of the force. The separation of stages consists of free-fall, impact, and submergence into the water.

Examining the time-histories of drag force, there is very little variation between grids during free-fall. All three curves are smooth, but the coarse grid begins to diverge from the other two at approximately 0.4 seconds. The difference between this grid and the other two only increases as time continues. The medium and fine grids, however, show close agreement during the entire fall, with only a 3.8% difference at 1.5 seconds, the end of this portion of the splashdown. It is worth noting here that the free-fall portion of the simulation is of lesser importance than the impact and even submergence. The pressures on the UAV during free-fall will be dwarfed by those seen at impact, so their effect on the structure is negligible. This, combined with the relatively small difference, suggests that the medium grid should be acceptable for the free-fall.
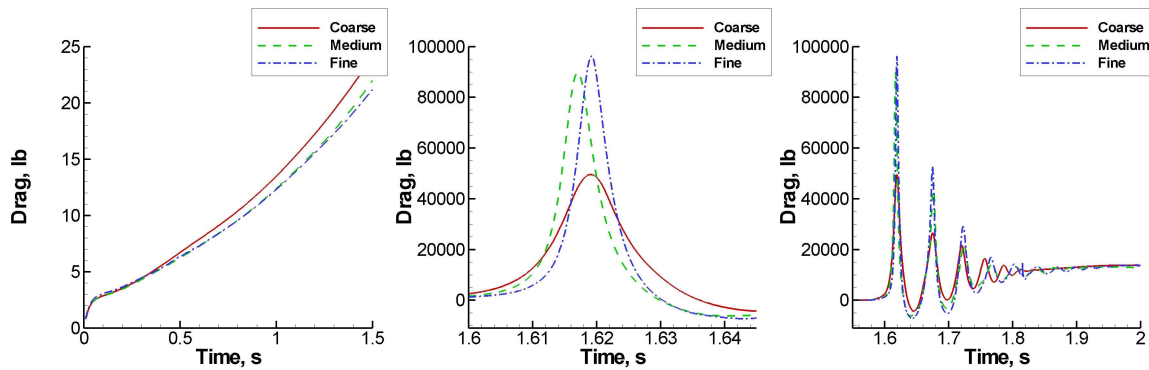
**Figure 7. Grid Independence for Free-Fall, Impact and Submergence**

The impact stage of splashdown follows a similar trend, with the medium and fine grids agreeing fairly well, and the coarse grid showing largely different results. Here the peak force for the coarse grid is much lower than the other two grids, and occurs over a longer period of time, yielding a short, wide curve. This is most likely due to insufficient resolution of the free-surface, where the diffusion mentioned earlier fails to produce a sharp spike at impact. The medium and fine grids have more the expected shape, with a high force for a short duration of time. There is a difference of 6.6% at the peak value, as well as some phase error at the time of impact. This can be partially explained by the difference during the free-fall. Since the Medium grid had higher drag during free-fall, it slowed a small amount more, and thus the impact speed was slightly lower. However, the agreement is still very close, so these two grids are very nearly grid-independent.

After impact, as the aircraft submerged into the water, there were oscillations in the drag force for all grids, on almost identical frequencies. The differences between the grids are present in the magnitude and damping of the oscillations. The coarse grid shows much lower magnitudes of force, and tends to damp out to a steady force much more quickly than either of the other grids. There are some small differences in magnitude and damping

between the medium and fine grids, but these are within an acceptable range for the two to be considered grid independent, and the period of oscillations are almost identical.

During the three phases of splashdown, free-fall, impact, and submergence, the medium and fine grids showed near-identical behavior in drag force. The coarse grid deviated a great deal from the other two. This shows that the medium grid is acceptable for further use, since grid refinement has almost no effect and coarsening drastically affects the solution. Note also that this study was done for the "worst-case" 40 ft drop, so impacts from lower heights should naturally be grid independent as well. Based on these results, the medium grid was selected for all successive simulations.

## 5.2  Effect of Drop Height

The Medium grid was used for simulations with the UAV dropped from various heights, corresponding to scheduled Lockheed Martin tests. These tests were performed for initial positions 10, 25, 35, and 40 ft above the water surface, as well as one test where the UAV was partially submerged. The nose of the aircraft began 3.6 ft below the surface, to quantify its buoyant characteristics. Finally, one simulation was performed for a drop from 65 ft height, which exceeded the range of the experimental testing. Since the grid independence study was performed for the 40 ft drop case, all of the Lockheed Martin test cases were sure to be grid independent. The 65 ft drop might have some inaccuracies due to grid, but this was not a required case, and was more of a "what-if" simulation. A list of all the simulations is given in Table 3, along with the corresponding velocity at impact for each case.

**Table 3.  Drop Height and Impact Velocity**

| Drop Height, $h$ | Impact Velocity. $V_{impact}$ |
|---|---|
| -3.6 ft | N/A |
| 10 ft | 25.4 ft/s |
| 25 ft | 40.1 ft/s |
| 35 ft | 47.5 ft/s |
| 40 ft | 50.7 ft/s |
| 65 ft | 64.7 ft/s |

Pressure time-histories were taken at various points on the aircraft body.  Figure 8

shows two of these plots, for the inlet door and the side of the inlet duct, for all drop heights.

Note that the plots have been shifted in time so impact occurs at t=0 for all cases to provide a

simpler comparison.  The same oscillations seen in the grid independence study are present

once more, but tend to dampen out by about 0.6 sec after impact.
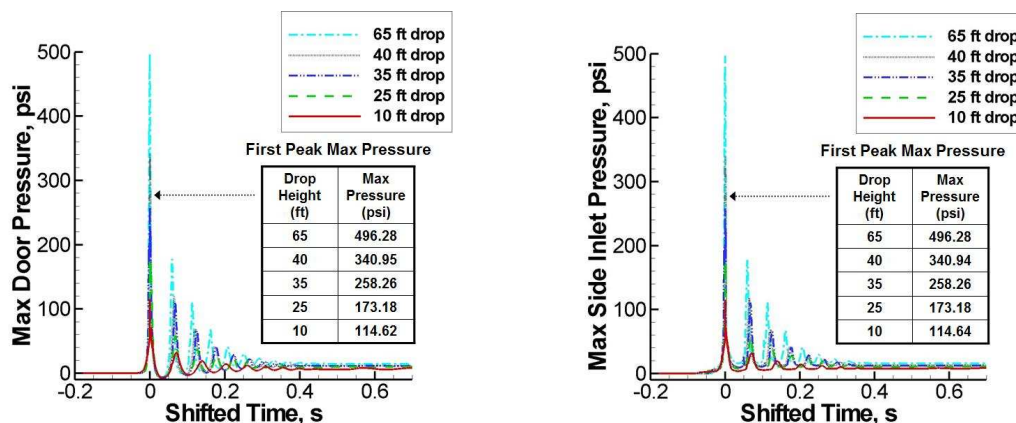


**Figure 8.  Maximum Static Pressure Histories on Inlet Sides and Inlet Close-off Door for Various Drop Heights**

For another perspective of this behavior, position, velocity and acceleration in the

vertical direction was recorded for the UAV as a whole.  These plots are given in Figure 9.

All drop height show the same character of splashdown behavior with variation in the

magnitudes of the position, velocity or acceleration being the only visible differences.  Here the acceleration graph exhibits the same oscillatory behavior shown in the pressure plots with the same damping effect as the UAV submerges.
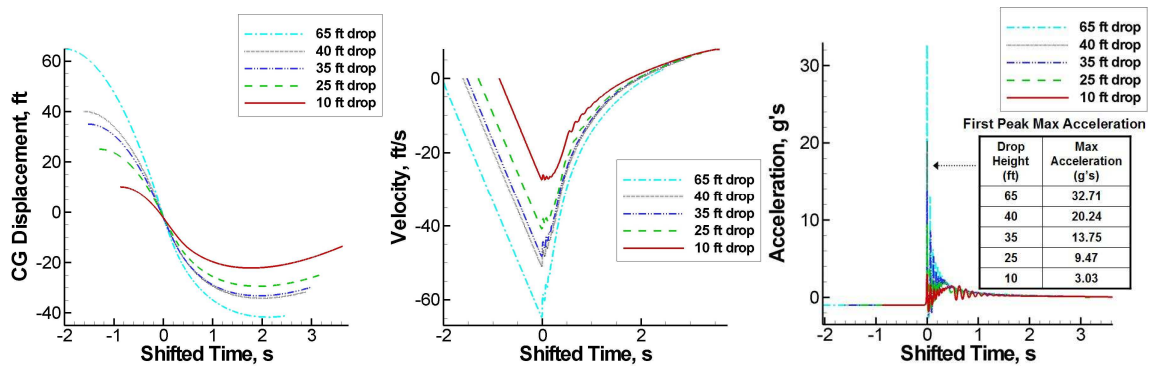


**Figure 9.  Vertical CG Position, Velocity and Acceleration for various Drop Heights**

An interesting point to note in both sets of plots is the fact that curves become negative in both pressure and acceleration.  Just after the peak pressure or acceleration, the measured quantity becomes negative for a short time, signifying a downward force and a suction pressure.  This is somewhat counterintuitive, but can be explained by the aircraft geometry and the physics of the splashdown.  This is best illustrated through a series of contour images at different times during the simulation.  Figure 10 shows the UAV at several discrete moments of interest for the 40 ft drop case.

The UAV first begins to pierce the surface of the water at 1.5923 seconds.  At this time, there is still air between the water surface and the inlet close-off door.  However, as the UAV plunges deeper into the water, this air is compressed, and some of it begins to escape out the sides of the inlet duct.  By 1.6002 seconds, the sides of the inlet duct have submerged into the water, closing off the exit route of the air, which compresses further into a bubble of air on the inlet door.  As the UAV sinks deeper into the water, hydrostatic pressures act on

this film of air, compressing it still more, until at 1.6107 seconds the maximum pressure is felt.  Finally the air cannot be compressed any further and expands outward in the only available direction, away from the door's surface.  This leads to a negative static pressure on the door, seen at 1.6293 seconds and discovered earlier in the pressure and acceleration plots.

The dynamics of the UAV continue as it sinks further into the water, again compressing the remaining air.  The air compresses again, reaches a lower peak value, and is expanded outward again.  This system of compression and expansion becomes a series of small "impacts" seen on the line plots as oscillations in pressure and acceleration.  The magnitudes decrease over time as air escapes out of the inlet duct and as the UAV slows its descent.  Once all of the air has been expelled, the oscillations stop.  Meanwhile, the UAV's descent through the water has left a column of air behind it, which eventually collapses at about the same time as the aircraft comes to a stop.  Its momentum has stopped, and now the water hydrostatic pressures return the buoyant UAV to the surface of the water.
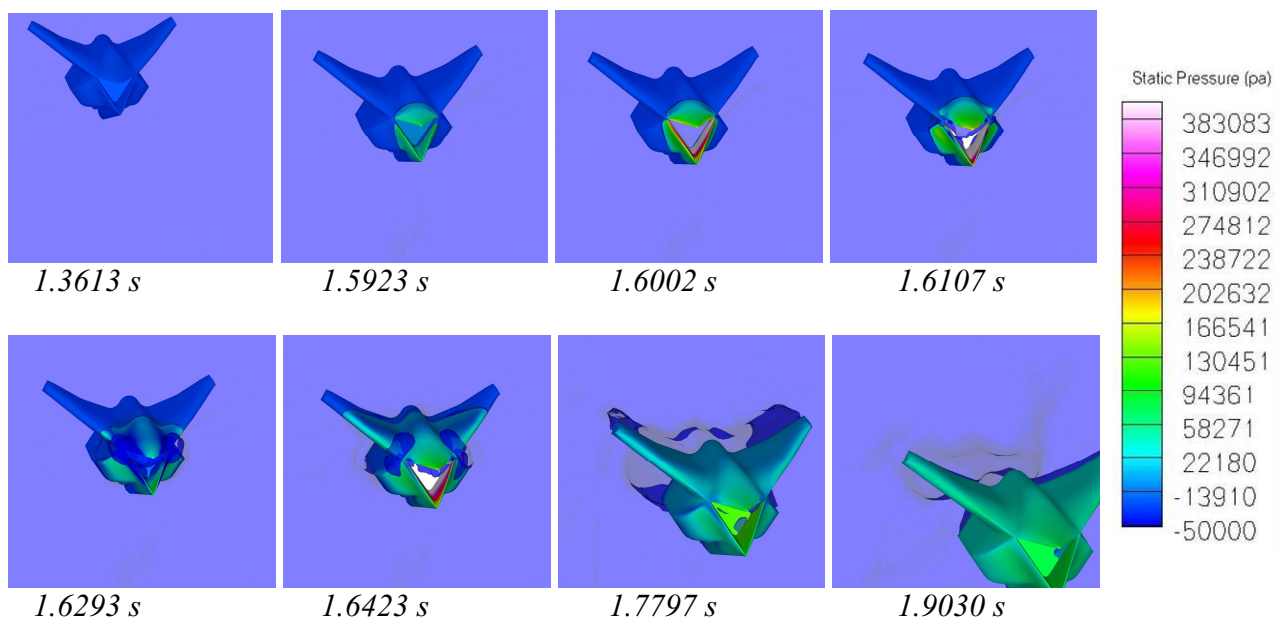


**Figure 10.  UAV Pressure Contours with Water Free Surface for 40 ft Splashdown**

## 5.3 Validation

The drop height study showed unique and counterintuitive behavior, which made it even more important to compare to experimental data. Lockheed Martin constructed a full scale test article, which closely matched the CFD geometry. This body was then dropped into the ocean from heights ranging from -3.6 ft to 25 ft. Pressure transducers recorded data at various locations on the aircraft during the entire splashdown. Comparisons between experimental and computational results for four key transducer locations are given here. The positions of these instruments are shown on the UAV body in Figure 11.
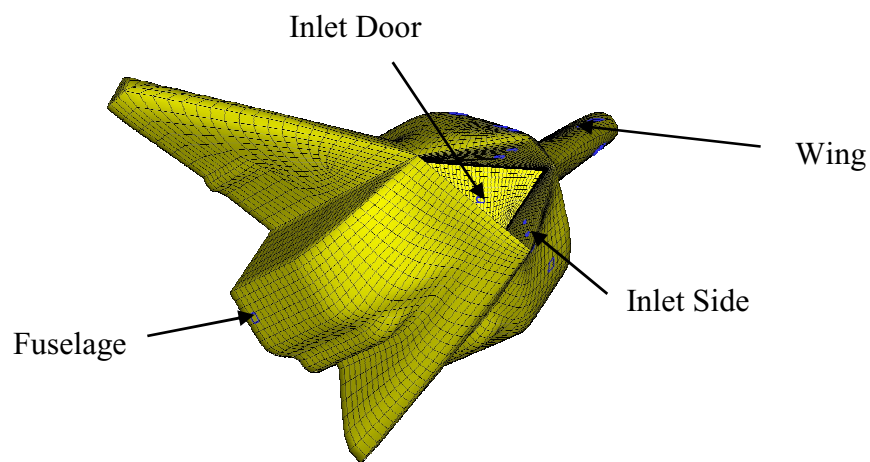
**Figure 11. Baseline Surface Grid with Pressure Transducer Locations**

The first comparison made was for the partially submerged case, begun with the nose 3.6 ft below the water's surface. In this position the aircraft's inlet duct is fully submerged, so the pressure oscillations seen previously should not be present. This is not the neutrally buoyant position for the UAV, so there were some dynamic effects caused by the offsetting forces of gravity and buoyancy. Essentially this test was performed to ensure that the computational model was correctly modeling these forces. For this case, the UAV sank due

to gravity until its nose was approximately 18.47 ft below the surface, then floated back up, bobbed somewhat and eventually came to rest at a neutrally buoyant depth. Figure 12 shows the comparison of computational and experimental results for this load case. Note that the fuselage pressure transducer had failed for this case, and its data was unavailable. The three available transducers show very close agreement to the CFD model, within 5% in magnitude for the three locations. This error could be caused by minor differences between actual and modeled fluid properties, but it small enough to be inconsequential.
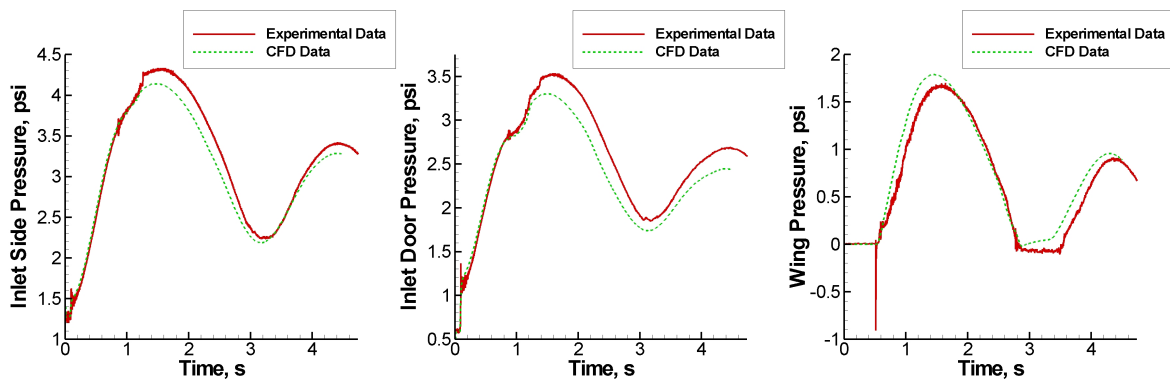


**Figure 12. Pressure History Comparison for -3.6 ft Drop**

The 10 ft drop case was tested next, with the comparison shown in Figure 13. There are two visible discrepancies between the experimental and computational results in the nose-area transducers. The CFD data under-predicts the peak pressure in the side of the inlet duct, and the oscillations are damped out much more quickly in the model than in the experiment. The wing and fuselage measurements correlate better in general, but the wing pressure transducer shows a sharply negative value just after impact. This could signify unresolved flow physics, or perhaps an errant transducer.
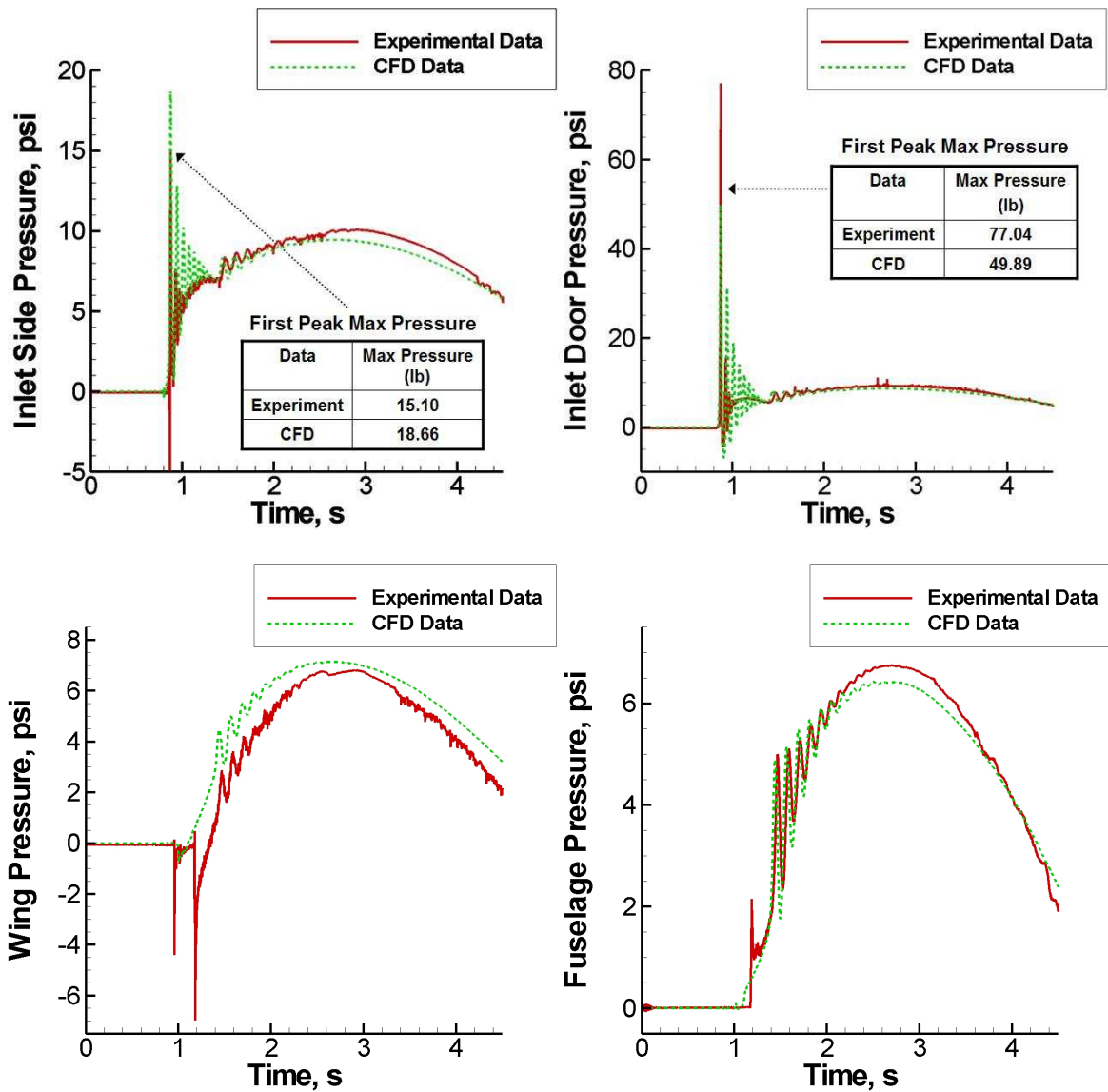
**Figure 13.  Pressure History Comparison for 10 ft Drop**

The 25ft drop case showed similar trends to the 10 ft case in areas of agreement as well as discrepancies.  Once more, the oscillations damped out faster in the computational model as compared to the test data.  The negative pressure on the wing after impact was again present as well.  However, the error seen previously with the model under-predicting duct pressure could not be verified for this load case, since the pressure transducer reached an operational limit and failed to read higher pressures.  Aside from these differences, the

general trends showed fairly good agreement with test data for all drop heights. These plots are shown in Figure 14.
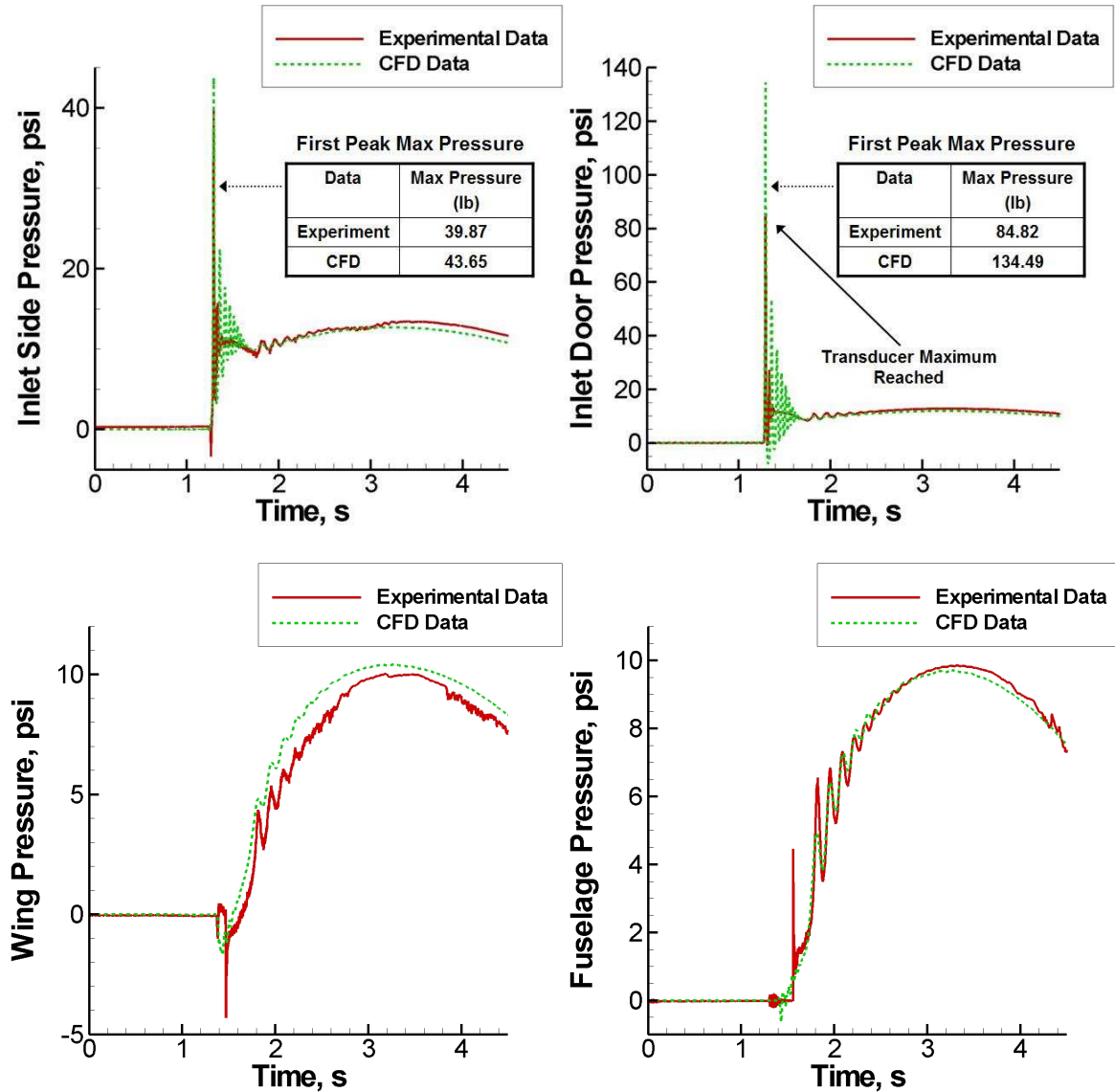


**Figure 14. Pressure History Comparison for 25ft Drop**

It is unknown exactly why these small discrepancies do exist, but there are a number of possible contributing factors. First, the conditions during the drop test were not precisely modeled in the CFD simulations. The experimental tests took place during a 1.5-2 kt wind, where the UAV was dropped into real seawater. Computationally, the wind was ignored, and

the fluids were idealized substances with typical properties.  It is also possible that the oscillations were damped out by vibrations in the aircraft material, which were not modeled in the rigid-body simulation.  Most likely, though, the differences are due to inherent inaccuracies and limitations of the VOF model.  Although this scheme can closely approximate the splashdown flow physics, the model is still not perfect.

As a final validation test, peak pressures and depths from all of the drop tests were collated onto one plot to evaluate trends of the model.  These are given in Figure 15.  This data was made available for the tests with pressure transducer data shown earlier, as well as additional tests that were performed later.  There is some scatter in these plots, as evidenced by the three disparate results found in 35 ft drop testing.  However, within a reasonable error bound, the values are close and the trends are very similar.  Both pressure and depth increase in a near-linear fashion with drop height, computationally and experimentally.  The CFD-generated pressure values lie to the lower end of the experimental data set, and the depth values are exact to within 3 ft.
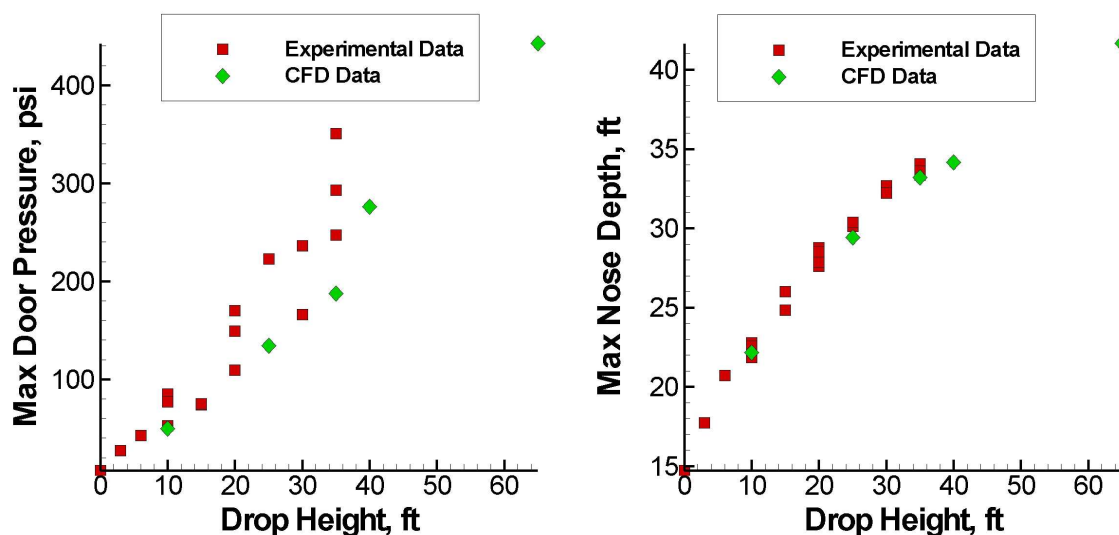


**Figure 15.  Maximum Inlet Close-Off Door Pressure and Maximum Plunge Depth**

## 5.4  Finite Element Analysis

In the course of validation testing performed by Lockheed Martin, the UAV inlet close-off door was damaged, being driven back into the duct by the force of impact.  This occurred for the 25 ft drop case, meaning a pressure of 204.2 psi caused the door to deflect.  Recall, though, that the door configuration for the test article was different from the actual aircraft, with three attachment points rather than a single arm.  Thus the damaged test door raised the question of whether a similar result would occur on the actual UAV.

The door mechanism was meshed in ANSYS as described in Chapter 3, and boundary conditions applied as in Chapter 2.  The ANSYS simulation was then able to run.  Initially the pressure was applied in a time-accurate fashion as output from Fluent to model the entire shock load.  This result was then compared to a steady-state computation using only the peak pressure value.  The stresses output by the two methodologies were nearly identical, so the less computationally expensive peak model was used for all subsequent evaluations.

The results of the FEA simulation showed high stresses, especially in the support arm.  In places, the stresses exceeded the yield strength of the material.  This necessitated the use of a nonlinear stress-strain curve for the stainless steel components.  Stresses in the titanium door never exceeded yield, so linear material properties were retained for this portion of the model.  Plots of the strain and deflection experienced by the assembly are shown in Figure 16 below.
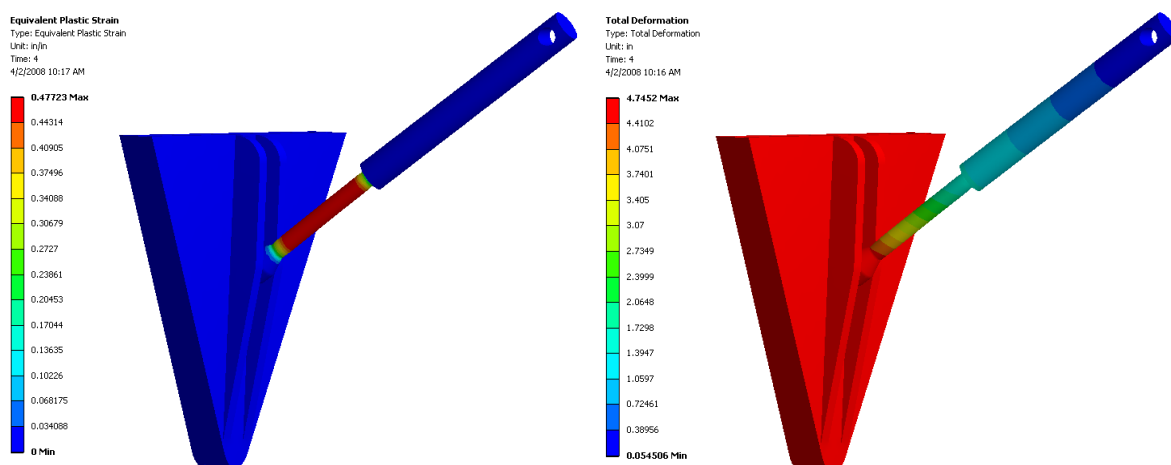
**Figure 16. Strain and Deformation plots for Inlet Door 25 ft drop**

Naturally, no strain is shown in the titanium portions of the door, since stresses there never exceeded yield.  However, there are significant strains in the arm, specifically in its narrower section.  Since stress is defined as a force applied over an area, it is expected that the smaller cross-sectional area would see the highest stresses, and thus the highest strains. Strain levels are significant, to a maximum value of 0.47723 in/in, which would be expected to buckle the stainless steel arm.

This is confirmed by investigating the deformation plot.  Maximum deformation of 4.7452 in occurs over the entire door.  The titanium of the door panels is too strong for it to fail, so it is simply pushed back as the arm fails behind it.  Since the door is constrained by the ductwork around it, it can only deflect into the arm, leaving the weaker material to take all of the strain.  This confirms the failure seen in experimental testing.

# CHAPTER 6.  SUMMARY AND CONCLUSIONS

Computational studies were performed for a UAV splashdown into water, utilizing CFD and FEA methods.  The CFD analyses used dynamic cell remeshing and the Volume of Fluid model in conjunction with the unsteady "incompressible" and "compressible" ensemble averaged Navier-Stokes equations to move the aircraft through the domain and into the water.  A variable time-stepping method was used to speed the simulations.

The study was verified by comparing to tests performed by Lockheed Martin for several different drop heights.  Pressure histories of these drops showed good agreement between experiment and computation, with some discrepancies noticed in the inlet duct. These differences were identified to be expansion and compression of the air in the duct cavity; although these occurred in tests, the magnitude of oscillation was much smaller than predicted.  This is most likely due to modeling deficiencies in the CFD method, but their effect on predicted pressure was quite small regardless.  Other transducer locations showed excellent agreement with experiment, as did the maximum depth and pressure compilations for varying drop heights.

The FEA simulation evaluated the inlet close-off door geometry for the 25 ft drop case, for which the test inlet door had failed.  The pressures output from the CFD analysis were applied to the meshed model and run using nonlinear MISO material data.  The results of the study showed high strains and deflections, mirroring the effects seen in experimental testing where the supports had buckled.  For future use in the aircraft, this inlet door mechanism should be redesigned or strengthened to withstand the impact forces of splashdown.

# BIBLIOGRAPHY

ANSYS 11.0 Users Guide (2007). *ANSYS, Inc.*

Armsfield, S and Street, R. (1999). The Fractional-Step Method for the Navier-Stokes Equations on Staggered Grids: Accuracy of Three Variations. *Journal of Computational Physics*, Vol. 153, 660-665.

Fluent 6.2 Users Guide (2005). *Fluent, Inc.*

Muzaferija, S., Peric, M., Sames, P., and Schellin, T. (1998). A Two Fluid Navier-Stokes Solver to Simulate Water Entry. *Proc 22$^{nd}$ Symposium on Naval Hydrodynamics*, Washington, DC, 277-289.

Von Karman, T. (1929). The Impact of Seaplane Floats During Landing. *NACA TN*, Vol. 321

Wagner, H. (1932). Ueber Stoss – und Gleitvorgange an der Oberache von Flussigkeiten. *ZAMM*, Band 4, Heft 4, 193-235.

Youngs, D.L. (1982). Time-Dependent Multi-Material Flow with Large Fluid Distortion. *Numerical Methods for Fluid Dynamics*.

# ACKNOWLEDGEMENTS